Monthly Notices of the ROYAL ASTRONOMICAL SOCIETY

MNRAS **460,** 212–226 (2016)
Advance Access publication 2016 April 21

doi:10.1093/mnras/stw937

Active galactic nuclei at $z \sim 1.5$ – III. Accretion discs and black hole spin

D. M. Capellupo,[1,2★] H. Netzer,[1] P. Lira,[3] B. Trakhtenbrot[4†] and J. Mejía-Restrepo[3]

[1] *School of Physics and Astronomy, Tel Aviv University, Tel Aviv 69978, Israel*
[2] *Department of Physics, McGill University, Montreal, Quebec H3A 2T8, Canada*
[3] *Departamento de Astronomía, Universidad de Chile, Camino del Observatorio 1515, Santiago, Chile*
[4] *Institute for Astronomy, Department of Physics, ETH Zurich, Wolfgang-Pauli-Strasse 27, CH-8093 Zurich, Switzerland*

Accepted 2016 April 19. Received 2016 April 18; in original form 2015 December 6

ABSTRACT

This is the third paper in a series describing the spectroscopic properties of a sample of 39 AGN at $z \sim 1.5$, selected to cover a large range in black hole mass (M_{BH}) and Eddington ratio (L/L_{Edd}). In this paper, we continue the analysis of the VLT/X-shooter observations of our sample with the addition of nine new sources. We use an improved Bayesian procedure, which takes into account intrinsic reddening, and improved M_{BH} estimates, to fit thin accretion disc (AD) models to the observed spectra and constrain the spin parameter (a_*) of the central black holes. We can fit 37 out of 39 AGN with the thin AD model, and for those with satisfactory fits, we obtain constraints on the spin parameter of the BHs, with the constraints becoming generally less well defined with decreasing BH mass. Our spin parameter estimates range from ~ -0.6 to maximum spin for our sample, and our results are consistent with the 'spin-up' scenario of BH spin evolution. We also discuss how the results of our analysis vary with the inclusion of *non-simultaneous GALEX* photometry in our thin AD fitting. Simultaneous spectra covering the rest-frame optical through far-UV are necessary to definitively test the thin AD theory and obtain the best constraints on the spin parameter.

Key words: accretion, accretion discs – galaxies: active – quasars: general.

1 INTRODUCTION

The dominant source of optical–UV emission in active galactic nuclei (AGN) is likely an accretion flow surrounding a central supermassive black hole (SMBH). For most cases, it is believed that this accretion flow takes the form of an optically thick, geometrically thin accretion disc (thin AD), as described in Shakura & Sunyaev (1973). The physics of an actively accreting BH is governed by three key parameters, namely its mass (M_{BH}), spin (defined using the dimensionless parameter a_*), and accretion rate ($\dot{M}$). These parameters are intimately connected to the nature of the accretion flow around the BH, and AGN with very large accretion rates are believed to have optically thick, geometrically thick accretion discs ('slim' ADs; Abramowicz et al. 1988; Ohsuga & Mineshige 2011; Netzer 2013, and references therein).

There are several 'standard' models in the literature that predict the emitted SED of thin ADs, based on the general ideas in Shakura & Sunyaev (1973) and with various improvements, including general relativistic (GR) corrections, radiative transfer in the disc atmosphere, and disc winds (e.g. Hubeny et al. 2001; Davis & Laor 2011; Done et al. 2012; Slone & Netzer 2012). As described in Koratkar & Blaes (1999) and Davis & Laor (2011), as well as in our previous paper, Capellupo et al. (2015) (hereafter, Paper I), early attempts to fit such thin AD models to observed AGN spectra have generally found that the theoretical SEDs are significantly bluer than those observed. However, these studies were likely affected by relatively narrow wavelength coverage, by potential variability between different observations taken by different instruments, and/or stellar light contamination at long wavelengths.

Furthermore, while estimates of M_{BH} and $\dot{M}$ (or the Eddington ratio, L/L_{Edd}) have been obtained for many active SMBHs, the spin parameters are largely unknown. Up until recently, spin measurements have been limited to X-ray observations of relatively nearby AGN that are able to probe the innermost regions of the AD. Specifically, high-quality X-ray observations are required to model the profile of the relativistic 6.4 keV Kα line, and such measurements have been performed for only a handful of AGN at low redshift (Fabian et al. 2000; Brenneman 2013; Risaliti et al. 2013; Reis et al. 2014; Reynolds 2014, and references therein). The highest redshift AGN with such a measurement so far is at $z \sim 0.6$, and this was possible only because it is lensed (Reis et al. 2014). A further downside to this approach is that these measurements cannot distinguish between negative spin and spin of 0 because the changes are too small in the broad 6.4 keV line profile. Therefore, a method that is sensitive to the full range of spin parameters ($-1 \leq a_* \leq 1$) and can be applied to AGN at larger redshifts is necessary.

★E-mail: danielc@physics.mcgill.ca
† Zwicky Postdoctoral Fellow.

In Paper I, we introduced a new sample of AGN, observed with a unique instrument, X-shooter, at the VLT (Vernet et al. 2011). This sample was selected based on the BH mass and the Eddington ratio ($L/L_{\rm Edd}$), two of the three fundamental properties of active BHs. Nothing was known about the spin of this sample at the time the sample was selected.

Our sample was selected in a narrow redshift range centred around $z \simeq 1.55$. This redshift was selected so that the four strongest broad emission lines (BELs; Hα, Hβ, Mg II 2800 Å, and C IV 1549 Å) would fall within the observed spectral range of the X-shooter instrument. This is important for addressing the physics of BELs and the estimation of $M_{\rm BH}$ based on these BELs. Using the X-shooter instrument avoids the problem of line and continuum variations that arises when observing individual BELs at different times and with different instruments. The results of this part of the project are described in Mejía-Restrepo et al. 2016 (hereafter, Paper II).

Our work in Paper I showed that with wide, single-epoch wavelength coverage of the SEDs, the thin AD theory is indeed consistent with the data for at least 25 out of the 30 AGN we studied, in contrast with many of the earlier works on AGN SED fitting. Furthermore, we were able to constrain the spin parameter for those sources with satisfactory thin AD fits to the SEDs.

In the current work, we improve and expand upon the work in Paper I in three ways. First, we add an additional nine AGN to the sample to fill a section of the $M_{\rm BH}-L/L_{\rm Edd}$ plane missing in Paper I, namely fainter AGN with a combination of smaller $M_{\rm BH}$ and lower $L/L_{\rm Edd}$. Secondly, we improve our Bayesian AGN SED fitting procedure by including improved $M_{\rm BH}$ estimates from Paper II and, instead of applying intrinsic reddening only to those AGN that could not otherwise be fit with a thin AD SED, as we did in Paper I, we now include an intrinsic reddening correction in our Bayesian fitting procedure for all sources. Third, we investigate the inclusion of archival photometry from *GALEX*, in order to extend our wavelength coverage further into the UV. This allows us to cover a larger portion of the AGN SED that is dominated by radiation from the AGN accretion disc. Although, this analysis is hampered by potential variability between the non-simultaneous *GALEX* and X-shooter observations.

We summarize the sample selection, observations, and data reduction in Section 2. In Section 3, we describe the thin AD model we use, our procedure for fitting the model to the data, and the results of fitting both the X-shooter spectra alone and the combined X-shooter+*GALEX* SEDs. In Section 4, we discuss the implications of our results on the nature of AGN accretion discs and our understanding of AGN BH spin evolution. Throughout this work, we assume a ΛCDM cosmological model with $\Omega_\Lambda = 0.7$, $\Omega_{\rm m} = 0.3$, and $H_0 = 70\,{\rm km\,s^{-1}\,Mpc^{-1}}$.

2 SAMPLE OBSERVATIONS AND DATA REDUCTION

2.1 X-shooter

In this work, we use a sample of AGN selected from the seventh data release of the SDSS (Abazajian et al. 2009), as described in Paper I, and from 2SLAQ (Croom et al. 2009). To summarize, our sample was selected to cover the widest possible range in $M_{\rm BH}$ and $L/L_{\rm Edd}$, within a narrow redshift range, $z \simeq 1.45$–1.65. For the purpose of selecting the sample only, we use measurements of the Mg II emission line in the SDSS (for the original 30 sources described in Paper I) and 2SLAQ (for the new nine sources presented here) spectra, along with a standard bolometric correction (BC) factor

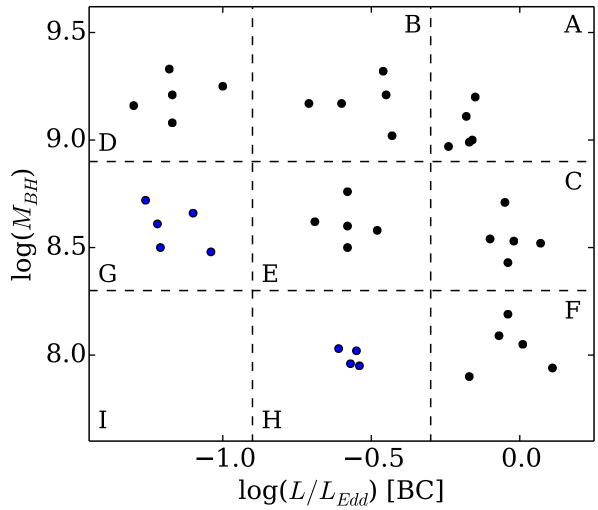

Figure 1. Our sample selection plotted on the $M_{\rm BH}$–$L/L_{\rm Edd}$ plane, using the measured values based on SDSS and 2SLAQ spectra and McLure & Dunlop (2004). Black points are the original 30 and blue points are the 9 new sources.

and relations given in McLure & Dunlop (2004), to estimate $M_{\rm BH}$ and $L/L_{\rm Edd}$. We divide the known $M_{\rm BH}-L/L_{\rm Edd}$ plane into nine bins, and we select five objects per bin (Fig. 1). We have currently observed 39 AGN, in bins A−H, with $M_{\rm BH}$ ranging from $\sim 9 \times 10^7$ to 4×10^9 M$_\odot$ and $L/L_{\rm Edd}$ from ∼0.04 to 0.7.

The X-shooter instrument at the VLT provides spectra with continuous wavelength coverage from ∼3000 to 25 000 Å, by simultaneously observing three wavelength regions, the UV-blue (UVB), visible (VIS), and near-infrared (NIR; Vernet et al. 2011). The instrumental set-up for the nine new sources presented in this paper (ESO programme 092.B-0613) is the same as for the original 30 (Paper I; ESO programme 088.B-1034). We observe with the widest available slit widths, 1.2–1.6 arcsec, giving a resolving power of 3300–5400, depending on the arm. Table 1 lists the nine new objects in our sample and the dates of observation.

The spectra were reduced using the ESO Reflex environment (Freudling et al. 2013) and version 2.5.2 of the ESO X-shooter pipeline, in nodding mode (Modigliani et al. 2010). The pipeline subtracts the detector bias and dark current, rectifies and calibrates the wavelength scale of the spectra, and uses an observed spectroscopic standard star spectrum to calculate an absolute flux-calibrated spectrum. In general, the standard star is observed the same night as the science target.

With the pipeline-calibrated result, we then corrected the spectra for telluric absorption within the VIS arm spectrum, using a telluric standard star observation at a similar airmass as the AGN observation taken either right before or right after the AGN observation. In the case of the wavelength region ∼8950–9800 Å, we used a model telluric spectrum instead of a standard star observation. In the NIR arm, where there is more significant telluric absorption, we simply remove the regions of the spectrum most affected by this absorption.

Finally, we use the Schlegel, Finkbeiner & Davis (1998) maps and Cardelli, Clayton & Mathis (1989) extinction law to correct the spectra for Galactic extinction. Table 1 lists the values of A_V due to the Galaxy for the nine new targets.

Fig. 2 shows the full X-shooter spectra of the nine new sources. All sources are corrected for Galactic extinction, and some have been corrected for host galaxy contamination, as described in

Table 1. Summary of observations and data reduction.

Name	Dates observed	A_V^a	Notes
J0042+0008	2013 October 24	0.02	^{b}
	2013 October 31		
J1021−0027	2014 February 23	0.05	^{c}
	2014 February 26		
	2014 February 27		
	2014 April 24		
	2014 April 24		
	2014 April 27		
J0038−0019	2013 November 03	0.02	^{b}
	2013 November 03		
	2013 November 04		
	2013 November 08		
J0912−0040	2013 December 31	0.03	^{b}
	2014 January 30		
J1048−0019	2014 April 27	0.04	^{b}
	2015 January 27		
	2015 January 27		
	2015 January 27		
J1045−0047	2014 March 08	0.04	
	2014 March 08		
	2014 April 23		
	2014 April 23		
	2014 April 24		
J0042−0011	2013 November 04	0.02	^{b}
	2013 November 08		
	2014 July 28		
	2014 July 28		
	2014 July 29		
	2014 July 29		
J1046+0025	2014 February 24	0.04	^{b}
	2014 February 26		
	2014 February 26		
	2014 February 27		
	2014 March 01		
	2014 March 01		
J0930−0018	2014 February 04	0.03	^{b}
	2014 February 22		
	2014 February 22		
	2014 February 23		

Notes. ^{a}Galactic extinction.
^{b}Requires host galaxy subtraction.
^{c}BALQSO.

Section 3.1. The spectra are ordered by source luminosity as determined from $\lambda L_\lambda(3000)$ Å. For consistency, the sources are ordered in this same way in Table 1.

2.2 *GALEX*

To increase our wavelength coverage, we incorporate measurements from the sixth and seventh data release of *GALEX*. The *GALEX* mission has surveyed the sky in two UV bands. The far-UV filter has a bandwidth of 1344–1786 Å, with an effective wavelength of 1538.6 Å, and the near-UV filter has a bandwidth of 1771–2831 Å, with an effective wavelength of 2315.7 Å (Morrissey et al. 2007). This corresponds to rest wavelengths of ∼600 and 900 Å for our sample. The *GALEX* catalogue contains photometric measurements of 38 out of 39 of the AGN in our sample in the NUV band and 20 in the FUV band. We have up to five epochs of *GALEX* photometry per source, taken anywhere from 2003 September to 2012 February. The first X-shooter observations from Paper I began in 2011 October, whereas 75 per cent of our sample only have *GALEX* data from before 2010. As detailed below, time variability is evident in many of these observations, so we consider all epochs here.

The *GALEX* magnitudes range from 17.7 to 23.5, and most of the errors range from 0.02 to 0.3 mag, with a few measurements having errors as high as 0.6 mag. We also corrected the *GALEX* measurements for Galactic extinction, using the same extinction maps and extinction law as for the X-shooter spectra.

3 FITTING ACCRETION DISC MODELS

3.1 Standard thin AD models

As described in Paper I, most current AD models are based on the blackbody thin disc model of Shakura & Sunyaev (1973), with two significant improvements: the inclusion of general relativity (GR) terms and the improvement of the radiative transfer in the disc atmosphere (e.g. Hubeny et al. 2001; Davis & Laor 2011). In the current paper, we continue to use the numerical code presented in Slone & Netzer (2012) to calculate thin AD spectra, with a viscosity parameter (α) of 0.1.

Before calculating thin AD models, we calculate both $M_{\rm BH}$ and $\dot{M}$ (the accretion rate in $M_\odot$ yr^{-1}) directly from the observed spectrum. A major improvement relative to Paper I is the use of new $M_{\rm BH}$ measurements based on the comparison of four strong emission lines in our own sample – Hα, Hβ, Mg II, and C IV (Paper II). The main results of Paper II are: (1) Hα, Hβ, and Mg II give consistent estimates of $M_{\rm BH}$, albeit with a normalization which is somewhat different from the one used in Paper I (based on the Trakhtenbrot & Netzer 2012 calibration of the Mg II method). The Mg II-based estimates are less reliable for broad absorption line AGNs and for sources where FWHM(Mg II) > FWHM(Hβ). (2) The C IV line by itself does not provide reliable BH mass estimates for many of the sources. (3) New estimates of $M_{\rm BH}$ that are based on the FWHM of Mg II are larger than the estimates used in Paper I by ∼0.16 dex, with a scatter of 0.20 dex. All calculations and model fitting presented in this paper use the new mass measurements.

The method for measuring $\dot{M}$, in units of $M_\odot$ yr^{-1}, is the same as in Paper I, and is based on the properties of thin ADs (Collin et al. 2002; Davis & Laor 2011) and the fact that thin AD SEDs can be described by a canonical power law of the form $L_\nu \propto \nu^{1/3}$ at long enough wavelengths. Using the measured $M_{\rm BH}$ and equation 1 from Paper I, we can determine the mass accretion rate directly from the monochromatic luminosity in a wavelength region along this power-law portion of the SED. The one additional unknown is the inclination of the disc with respect to our line of sight.

The nine new sources presented here are fainter than the 30 sources presented in Paper I, and therefore, they are more susceptible to host galaxy contamination at longer wavelengths, including the wavelength region used for measuring the accretion rate. We therefore have to subtract the host galaxy emission in order to more accurately measure the AGN SED.

We determine which objects require a host galaxy subtraction based on the rest-wavelength equivalent width (EW) of the Hα emission line. The EW of the Balmer lines is not affected by the Baldwin effect, and the Hα line intensity is a reliable bolometric luminosity indicator (Stern & Laor 2012). We first look at the EW distribution of the brightest 28 AGN in the sample, whose luminosity at 5100 Å is high enough that host contamination is small enough to safely be neglected (Shen et al. 2011). We then compare the EW distribution for the 11 faintest AGN in the sample to the distribution for the brighter AGN, and we find most of the faint AGN have EW smaller than the median EW of the brighter AGN

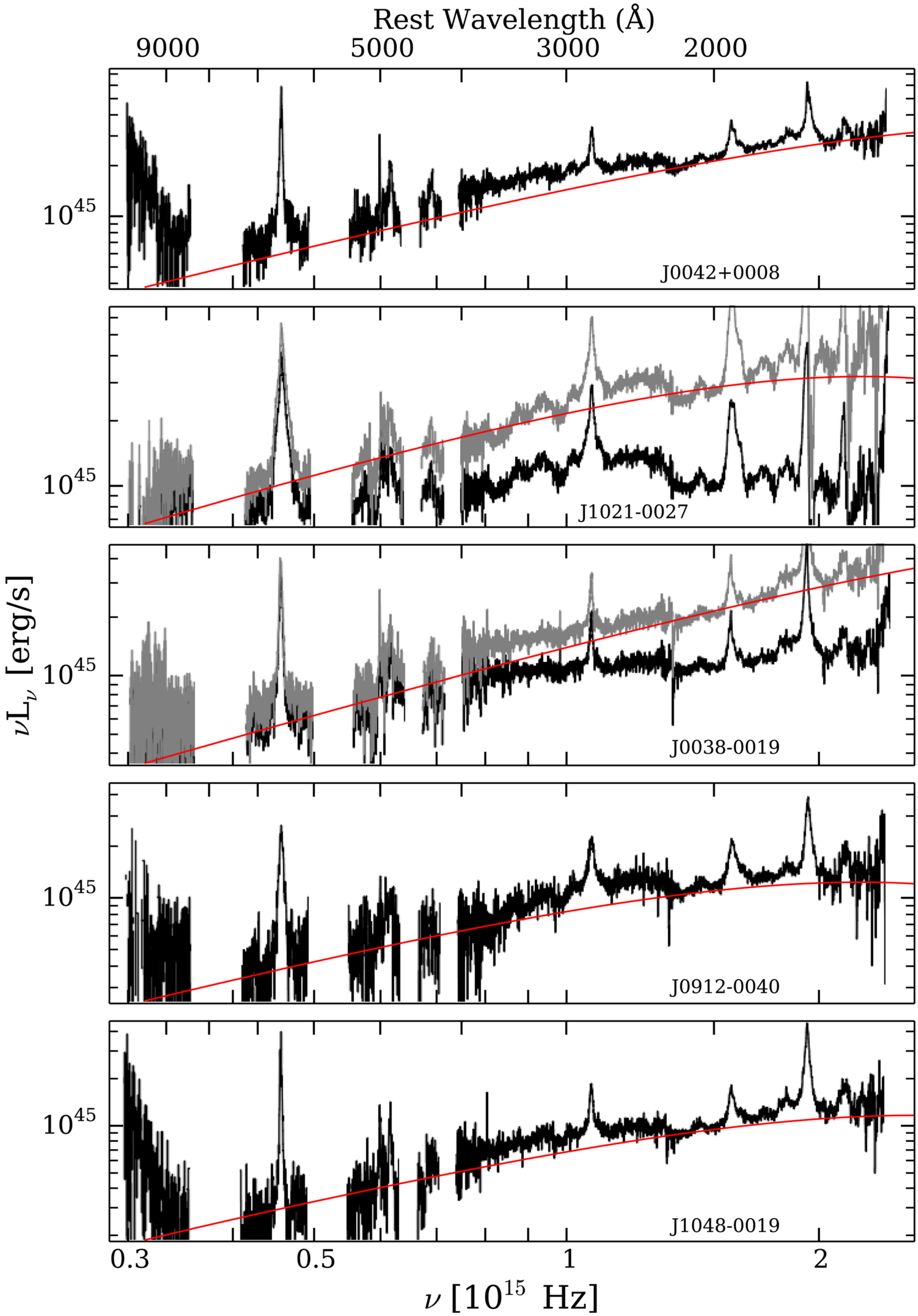

Figure 2. Spectra of the nine new X-shooter sources with the best-fitting thin AD models (red curves) overplotted. For those objects whose best model fit required an intrinsic reddening correction, we plot the dereddened spectrum in grey. Seven of the nine spectra were corrected for host galaxy contribution before fitting. The objects are ordered by source luminosity, as determined from $\lambda L_\lambda(3000)$ Å.

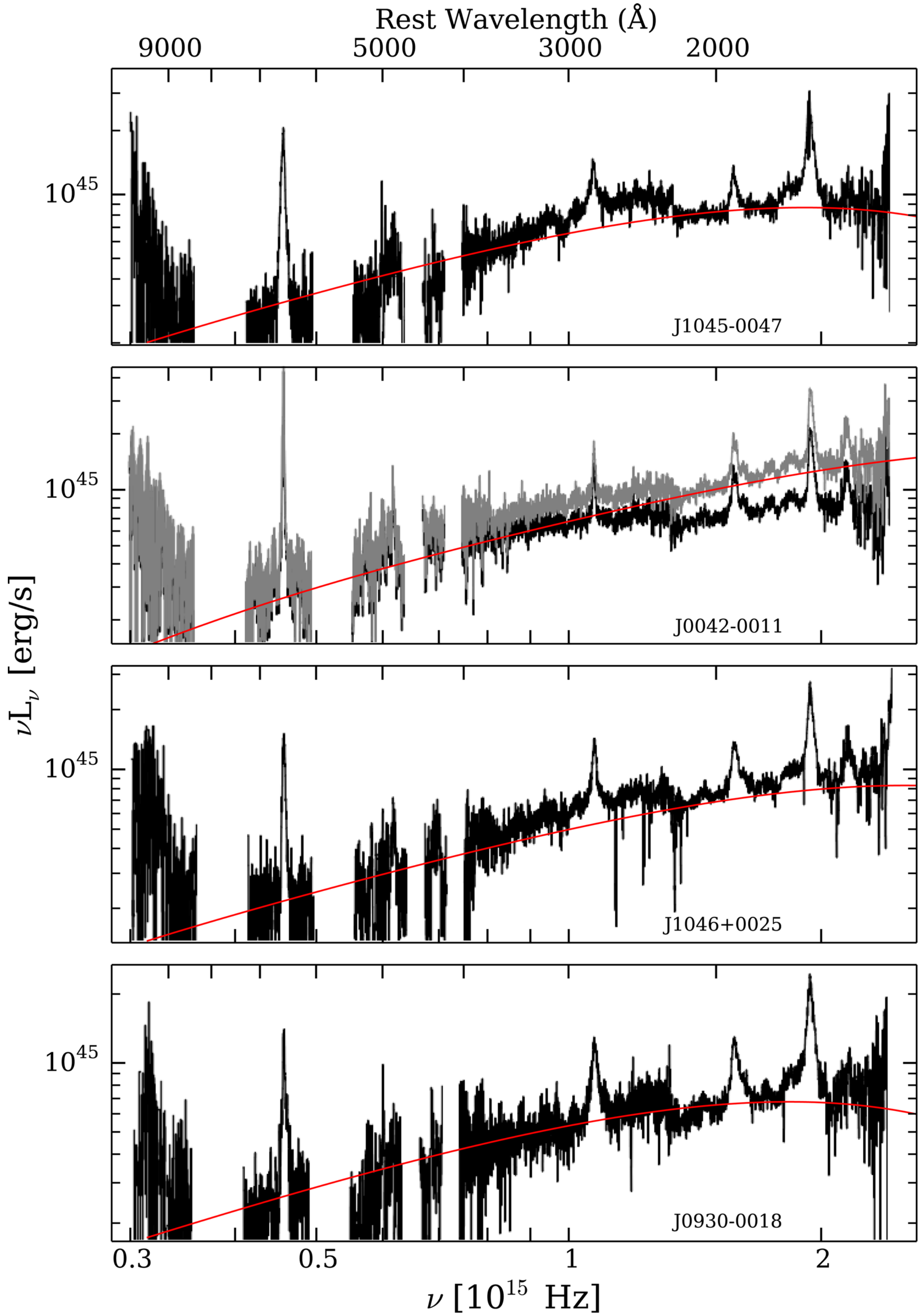

Figure 2. – *continued*

(i.e. EW < 400 Å). This clustering of AGN at low EW, as compared to the distribution of EW for the brighter sample, indicates there is host galaxy light raising the observed continuum luminosity in this wavelength region for these few objects.

In order to subtract the host galaxy for these few faint objects, we use a Bruzual & Charlot (2003) model of an old stellar population, with an age of 11 Gyr and solar metallicity. Such stellar population models have been used in many earlier works to correct for host

Table 2. Parameter values for the grid of AD models.

Parameter	Δ	Min-Max values
$\log M_{\rm BH}$ [M$_\odot$]	0.075	7.40: 10.25
$\log \dot{M}$ [M$_\odot$ yr^{-1}]	0.075	− 1.50: +2.10
a_*	0.1	− 1.0: +0.998
cosθ(1+2cosθ)/3	0.067	1.000: 0.330
A_V (mag)	0.05	0.00: 0.50

galaxy contamination (e.g. Bongiorno et al. 2014; Banerji et al. 2015). We scale the stellar population model based on the ratio between the observed Hα EW and the median of the EW distribution (400 Å). Younger stellar populations have a larger contribution in the UV, but using a stellar population with an age of 900 Myr, instead of the 11 Gyr model, changes the luminosity by less than 5 per cent at 3000 Å in the corrected AGN spectrum. Therefore, the choice of stellar population model does not have a large effect on the UV spectrum of our AGN. We now use these corrected spectra for measuring $\dot{M}$ and for the remainder of the analysis in this paper.

3.2 Bayesian SED-fitting procedure

We again generate a grid of thin AD models using the Slone & Netzer (2012) code, and we use a Bayesian method to fit the models to the observed spectra, in order to take into account the errors in $M_{\rm BH}$ and $\dot{M}$ and the unknown disc inclination. We use the same method described in Paper I, except that the grid now extends to lower $M_{\rm BH}$ and we now have a finer spacing in $M_{\rm BH}$ and $\dot{M}$ values (0.075 dex, instead of 0.15 dex; see Table 2). The expanded grid now includes 441 441 models.

In Paper I, we explored applying an intrinsic reddening correction to those AGN spectra that were not initially well fit by the thin AD model. However, it is possible that some of the AGN whose spectra are well fit are also affected by some amount of intrinsic reddening. We therefore add intrinsic reddening as another parameter in the Bayesian analysis. We adopt a range in A_V from 0. to 0.50 mag, in intervals of 0.05. To minimize the number of parameters, we adopt only a simple power-law curve, where $A(\lambda) = A_o\lambda^{-1}$ mag, to deredden the X-shooter spectra. To deredden the *GALEX* photometry, we use the MRN dust extinction model (Mathis, Rumpl & Nordsieck 1977).

To summarize our Bayesian approach, we determine the posterior probability for each of the 441 441 models for each value of A_V for each source. This probability is the product of the likelihood, $\mathcal{L}(m)$, and the priors on $M_{\rm BH}$ and $\dot{M}$. We have no prior knowledge on a_*, cos θ,[1] or the amount of intrinsic reddening. The likelihood is based on the standard χ^2 statistic, measured using up to seven line-free continuum windows, centred at 1353, 1464, 2200, 4205, 5100, 6205, and 8600 Å. The widths of these bands range from 10 to 50 Å. For five objects at the upper end of the narrow redshift range of our sample, the bands centred on 4205 and 5100 Å fall within regions of strong atmospheric absorption and are thus unusable. When calculating χ^2, we combine the standard error from Poisson noise and an assumed 5 per cent error on the flux calibration.

We use Gaussian distributions, centred on the observed values ($M_{\rm BH}^{\rm obs}$, $\dot{M}^{\rm obs}$) and with standard deviations (σ_M, $\sigma_{\dot{M}}$) given by their uncertainties, to represent the priors on $M_{\rm BH}$ and $\dot{M}$. We again adopt 0.3 and 0.2 dex for σ_M and $\sigma_{\dot{M}}$, respectively. The resulting posterior probability is given by

$$\text{posterior} \propto \exp(-\chi^2/2) \times \exp(-(M_{\rm BH}^{\rm obs} - M_{\rm BH}^{\rm mod})^2/2\sigma_M^2) \times \exp\left(-\left(\dot{M}^{\rm obs} \times \frac{M_{\rm BH}^{\rm obs}}{M_{\rm BH}^{\rm mod}} - \dot{M}^{\rm mod}\right)^2 /2\sigma_{\dot{M}}^2\right).$$

Appendix A in Paper I gives the full derivation of the posterior probability.

The Bayesian procedure ranks the 441 441 models based on the posterior probability for each one. We consider an AGN to have a satisfactory thin AD fit when the model with the highest probability has a reduced χ^2 statistic less than 3.

3.3 Fitting X-shooter spectra

We first fit thin AD models to just the X-shooter spectra for all the sources. From Paper I, 22 out of 30 AGN have a satisfactory fit, before making any additional corrections to the spectra (i.e. correcting for intrinsic reddening or considering disc winds). After correcting for intrinsic reddening, but using only a single value of A_V per source, we found satisfactory fits to another 3 out of 30 sources, bringing the total to 25 out of 30 AGN.

Using a larger model grid and considering multiple values of A_V, we find that 37 out of the entire sample of 39 AGN have satisfactory fits. Three of the AGN with marginal fits in Paper I can now be fit satisfactorily, and all of the nine AGN we add to the sample in the current work have satisfactory fits. Only one of the nine new sources (J1021-0027) requires an intrinsic reddening correction for a satisfactory fit (in total, 6 of the 39 sources require such a correction for a satisfactory fit). The best-fitting models for the nine new sources are overplotted in Fig. 2.

In Fig. 3, we show the probability contours for two of the five parameters, a_* versus $M_{\rm BH}$, for the 37 AGN with satisfactory fits to the X-shooter spectrum. The six sources that can only be fit after dereddening the spectra are highlighted in red. Table 3 lists the median values of the deduced parameters based on the probabilities.

3.4 Fitting X-shooter+*GALEX* SEDs

While X-shooter provides excellent wavelength coverage, we are missing a significant portion of the AGN SED that is dominated by emission from the accretion disc. In particular, we are missing wavelengths bluewards of ∼1200 Å, where, in most cases, a turnover in the thin AD spectrum occurs. Some constraint on the AGN SED at these short wavelengths is necessary to fully test the thin AD theory and constrain the various input parameters via the Bayesian method we adopt.

One solution that is already readily available is the *GALEX* survey. As described in Section 2.2, the latest data release of *GALEX* contains photometric data for all but one of our sources at ∼900 Å, and for 20 out of 39 at ∼600 Å. However, there are two main caveats to the usage of *GALEX* photometry. The first is that the *GALEX* bands are very broad, and we cannot properly take into account any emission lines or potential intervening Lyα absorption that could affect the flux at these wavelengths. The second caveat is variability between the *GALEX* and X-shooter epochs, especially given that variability is known to be more significant at these short wavelengths (MacLeod et al. 2012; Zuo et al. 2012).

With these caveats in mind, we apply our Bayesian method to a combined X-shooter+*GALEX* SED. The procedure is the same as in Section 3.3, but we now have up to nine continuum regions, instead of seven. Because we have multiple epochs of *GALEX* photometry

[1] We only consider cos θ > 0.5, appropriate for type-I AGN.

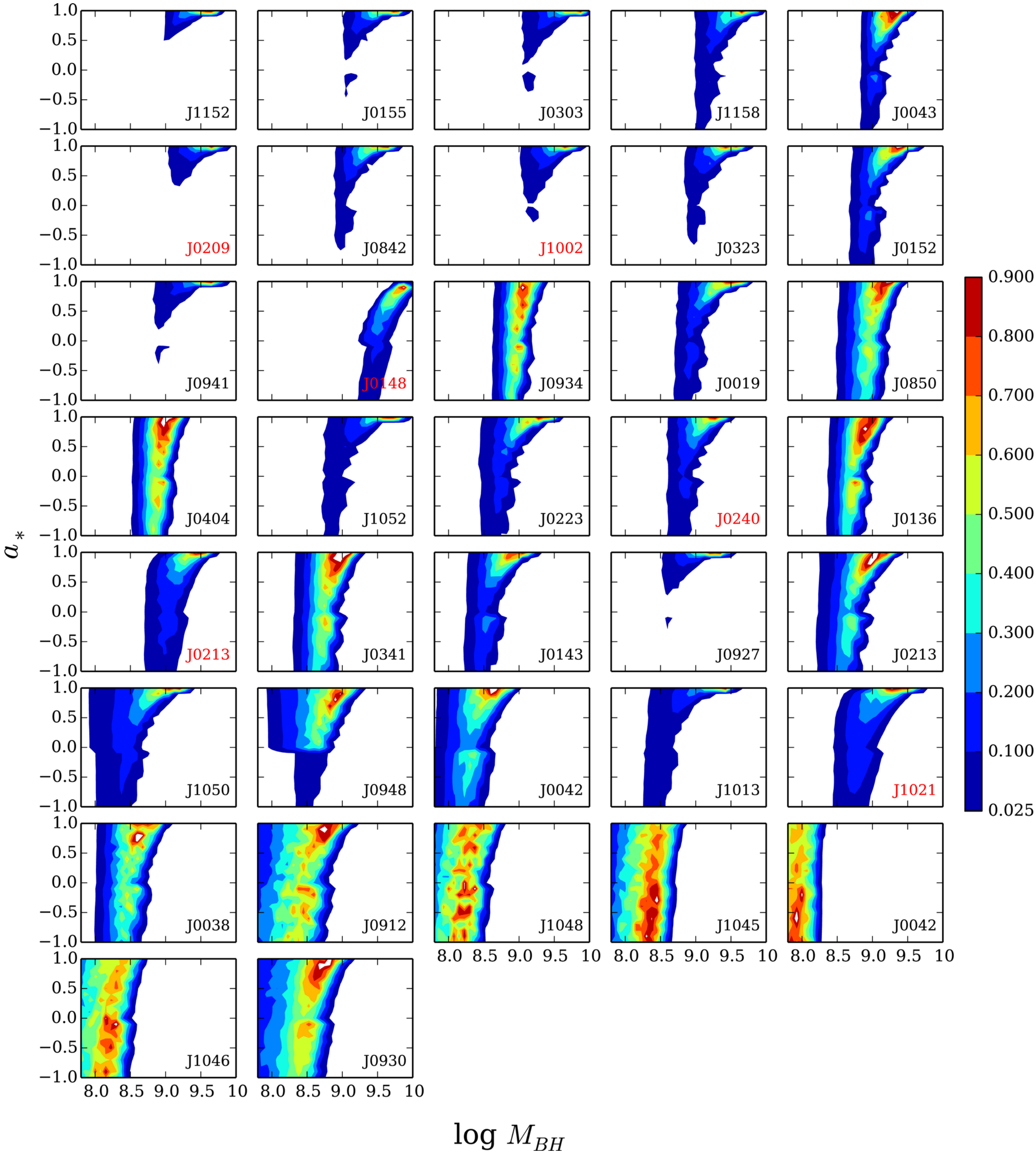

Figure 3. Contour plots of spin parameter a_* versus $M_{\rm BH}$ for the 37 sources with satisfactory fits to just the X-shooter spectrum. The objects labeled with red typeface are those sources which require an intrinsic reddening correction to obtain a satisfactory fit. The darkest blue contours correspond to a probability of less than 10 per cent.

for most sources, we use the weighted average of all the epochs for each source. For the error on each *GALEX* measurement, we combine the standard measurement errors with an extra error of 20 per cent to take into account the unknown variability between the X-shooter and *GALEX* epochs and an additional 5 per cent error based on the unknown slope of the SED through the *GALEX* filters. The error estimate for the unknown variability is based on the typical variability amplitudes found by MacLeod et al. (2012) and Zuo et al. (2012) and the variability between individual *GALEX* epochs in our own sample.

In Figs 4 and 5, we show several representative examples of the X-shooter+*GALEX* SED, with the best-fitting model shown in red and the best-fitting model to the X-shooter spectrum alone shown in blue. The coloured points are the individual *GALEX* epochs, and the

Table 3. Measured and deduced physical parameters.

Name	SDSS coord. name	log(L3000) [erg s^{-1}]	log M_{BH} [M$_\odot$] Obs.	log M_{BH} Xsh	log M_{BH} Xsh-GAL	log $\dot{M}$ [M$_\odot$ yr^{-1}] Obs.	log $\dot{M}$ Xsh	log $\dot{M}$ Xsh-GAL	logL/L_{Edd} [BC]	log $\dot{m}$ Xsh	log $\dot{m}$ Xsh-GAL	cosθ Xsh	cosθ Xsh-GAL	a_* Xsh	a_* Xsh-GAL	A_V Xsh	A_V Xsh-GAL	log(L5100) [erg s^{-1}]	log(L_{Bol})[a] [erg s^{-1}]
J1152+0702	J115239.68+070222.0	46.549	9.52	$9.46^{+0.20}_{-0.28}$	$9.18^{+0.18}_{-0.14}$	0.70	$0.84^{+0.31}_{-0.21}$	$1.33^{+0.30}_{-0.30}$	− 0.66	− 0.66	− 0.47	0.87	0.76	$0.980^{+0.048}_{-0.120}$	$0.152^{+0.625}_{-0.700}$	$0.00^{+0.02}_{-0.02}$	$0.00^{+0.02}_{-0.02}$	46.082	46.866
J0155−1023	J015504.74−102328.4	46.428	9.54	$9.45^{+0.28}_{-0.29}$		0.66	$0.80^{+0.30}_{-0.32}$		− 0.81	− 0.76		0.87		$0.960^{+0.061}_{-0.301}$		$0.05^{+0.05}_{-0.05}$		45.930	46.718
J0303+0027	J030342.79+002700.6	46.372	9.69	$9.54^{+0.30}_{-0.36}$	$9.44^{+0.46}_{-0.28}$	0.44	$0.71^{+0.37}_{-0.34}$	$0.80^{+0.35}_{-0.55}$	− 1.01	− 0.94	− 0.99	0.86	0.86	$0.960^{+0.061}_{-0.434}$	$0.767^{+0.224}_{-0.869}$	$0.08^{+0.06}_{-0.07}$	$0.01^{+0.04}_{-0.03}$	46.196	46.413
J1158−0322	J115841.37−032239.9	46.357	9.49	$9.37^{+0.29}_{-0.24}$		0.58	$0.83^{+0.31}_{-0.31}$		− 0.83	− 0.84		0.86		$0.828^{+0.172}_{-0.776}$		$0.10^{+0.07}_{-0.09}$		46.127	46.646
J0043+0114	J004315.07+011445.8	46.272	9.10	$9.15^{+0.18}_{-0.16}$	$9.11^{+0.16}_{-0.12}$	0.90	$0.83^{+0.25}_{-0.24}$	$0.94^{+0.22}_{-0.26}$	− 0.52	− 0.66	− 0.75	0.87	0.86	$0.772^{+0.207}_{-0.824}$	$0.280^{+0.477}_{-0.748}$	$0.06^{+0.05}_{-0.06}$	$0.01^{+0.04}_{-0.03}$	46.109	46.642
J0209−0947	J020951.09−094727.3	46.263	9.45	$9.46^{+0.22}_{-0.27}$	$9.39^{+0.29}_{-0.24}$	0.62	$0.63^{+0.30}_{-0.25}$	$0.72^{+0.30}_{-0.30}$	− 0.76	− 0.93	− 0.97	0.88	0.87	$0.964^{+0.059}_{-0.277}$	$0.827^{+0.166}_{-0.600}$	$0.15^{+0.05}_{-0.09}$	$0.09^{+0.08}_{-0.07}$	45.792	46.566
J0842+0151	J084240.64+015134.1	46.226	9.39	$9.29^{+0.30}_{-0.25}$	$9.18^{+0.24}_{-0.17}$	0.42	$0.65^{+0.30}_{-0.31}$	$0.78^{+0.27}_{-0.29}$	− 0.86	− 0.86	− 0.88	0.86	0.84	$0.900^{+0.112}_{-0.486}$	$0.550^{+0.322}_{-0.870}$	$0.07^{+0.05}_{-0.06}$	$0.01^{+0.03}_{-0.02}$	46.093	46.417
J1002+0331	J100248.16+033155.9	46.195	9.44	$9.44^{+0.24}_{-0.26}$		0.53	$0.64^{+0.30}_{-0.27}$		− 0.82	− 0.98		0.86		$0.929^{+0.087}_{-0.466}$		$0.20^{+0.06}_{-0.11}$		46.112	46.643
J0323−0029	J032349.53−002949.8	46.153	9.32	$9.27^{+0.26}_{-0.26}$	$9.22^{+0.37}_{-0.26}$	0.44	$0.62^{+0.31}_{-0.29}$	$0.66^{+0.32}_{-0.41}$	− 0.73	− 0.85	− 0.88	0.87	0.87	$0.912^{+0.102}_{-0.490}$	$0.816^{+0.171}_{-0.533}$	$0.10^{+0.05}_{-0.08}$	$0.08^{+0.04}_{-0.05}$	45.786	46.570
J0152−0839	J015201.24−083958.2	46.116	9.24	$9.08^{+0.28}_{-0.21}$		0.44	$0.71^{+0.29}_{-0.32}$		− 0.81	− 0.75		0.85		$0.738^{+0.244}_{-0.944}$		$0.06^{+0.06}_{-0.06}$		46.033	46.421
J0941+0443	J094126.50+044328.8	46.083	9.59	$9.36^{+0.29}_{-0.40}$	$9.18^{+0.54}_{-0.23}$	0.03	$0.40^{+0.39}_{-0.33}$	$0.59^{+0.31}_{-0.57}$	− 1.19	− 1.06	− 1.03	0.85	0.85	$0.966^{+0.057}_{-0.392}$	$0.628^{+0.349}_{-0.992}$	$0.05^{+0.06}_{-0.05}$	$0.00^{+0.02}_{-0.02}$	45.866	46.188
J0148+0003	J014812.83+000322.9	46.059	9.61	$9.65^{+0.22}_{-0.21}$		0.36	$0.69^{+0.29}_{-0.27}$		− 0.91	− 1.42		0.85		$0.585^{+0.299}_{-0.669}$		$0.44^{+0.06}_{-0.11}$		45.676	46.481
J0934+0005	J093411.15+000519.7	45.939	8.84	$8.97^{+0.13}_{-0.14}$	$9.07^{+0.08}_{-0.06}$	0.66	$0.64^{+0.23}_{-0.21}$	$0.59^{+0.14}_{-0.11}$	− 0.58	− 0.91	− 1.25	0.88	0.91	$0.280^{+0.558}_{-0.800}$	$-0.551^{+0.460}_{-0.348}$	$0.10^{+0.09}_{-0.08}$	$0.00^{+0.02}_{-0.02}$	45.829	46.150
J0019−1053	J001946.98−105313.4	45.791	9.33	$9.14^{+0.33}_{-0.25}$	$9.09^{+0.26}_{-0.16}$	0.03	$0.27^{+0.32}_{-0.35}$	$0.35^{+0.25}_{-0.33}$	− 1.21	− 1.20	− 1.30	0.85	0.85	$0.797^{+0.200}_{-0.948}$	$0.346^{+0.513}_{-0.869}$	$0.09^{+0.10}_{-0.08}$	$0.02^{+0.05}_{-0.03}$	45.991	46.048
J0850+0022	J085027.88+002255.0	45.742	8.89	$8.96^{+0.17}_{-0.19}$		0.51	$0.52^{+0.28}_{-0.26}$		− 0.82	− 1.01		0.86		$0.293^{+0.580}_{-0.836}$		$0.20^{+0.11}_{-0.12}$		45.945	46.271
J0404−0446	J040414.14−044649.8	45.729	8.76	$8.90^{+0.14}_{-0.15}$	$8.90^{+0.13}_{-0.13}$	0.65	$0.56^{+0.24}_{-0.21}$	$0.56^{+0.23}_{-0.21}$	− 0.70	− 0.92	− 0.97	0.87	0.87	$0.291^{+0.571}_{-0.824}$	$0.099^{+0.619}_{-0.711}$	$0.15^{+0.09}_{-0.09}$	$0.13^{+0.09}_{-0.08}$	45.177	46.493
J1052+0236	J105213.24+023606.0	45.722	9.59	$9.26^{+0.42}_{-0.38}$	$9.28^{+0.44}_{-0.37}$	− 0.38	$0.10^{+0.41}_{-0.45}$	$0.07^{+0.42}_{-0.46}$	− 1.54	− 1.39	− 1.50	0.85	0.85	$0.897^{+0.117}_{-0.933}$	$0.854^{+0.156}_{-0.975}$	$0.11^{+0.11}_{-0.09}$	$0.09^{+0.08}_{-0.07}$	45.119	45.746
J0223−0007	J022321.39−000733.7	45.681	9.17	$8.90^{+0.35}_{-0.25}$	$8.95^{+0.23}_{-0.15}$	− 0.24	$0.28^{+0.32}_{-0.36}$	$0.31^{+0.23}_{-0.28}$	− 1.16	− 0.99	− 1.23	0.85	0.84	$0.749^{+0.239}_{-0.886}$	$0.254^{+0.536}_{-0.804}$	$0.06^{+0.08}_{-0.06}$	$0.00^{+0.02}_{-0.02}$	45.084	45.970
J0240−0758	J024028.85−075843.5	45.678	9.04	$8.98^{+0.25}_{-0.21}$		0.12	$0.24^{+0.29}_{-0.29}$		− 0.94	− 1.10		0.86		$0.756^{+0.233}_{-0.888}$		$0.12^{+0.09}_{-0.09}$		45.404	46.196
J0136−0015	J013652.44−001524.5	45.650	8.75	$8.76^{+0.17}_{-0.16}$	$8.77^{+0.15}_{-0.13}$	0.25	$0.36^{+0.25}_{-0.26}$	$0.37^{+0.23}_{-0.24}$	− 0.77	− 0.94	− 1.03	0.86	0.86	$0.379^{+0.494}_{-0.858}$	$0.082^{+0.636}_{-0.685}$	$0.06^{+0.08}_{-0.06}$	$0.04^{+0.07}_{-0.04}$	45.437	45.717
J0213−1003	J021350.45−100300.4	45.616	9.11	$9.16^{+0.26}_{-0.23}$	$9.22^{+0.24}_{-0.31}$	0.29	$0.33^{+0.32}_{-0.30}$	$0.28^{+0.34}_{-0.28}$	− 0.84	− 1.25	− 1.07	0.86	0.86	$0.658^{+0.318}_{-0.921}$	$0.956^{+0.064}_{-0.401}$	$0.38^{+0.10}_{-0.15}$	$0.46^{+0.04}_{-0.08}$	45.281	46.123
J0341−0037	J034156.07−003706.4	45.572	8.76	$8.77^{+0.18}_{-0.18}$	$8.75^{+0.18}_{-0.15}$	0.25	$0.32^{+0.27}_{-0.27}$	$0.34^{+0.25}_{-0.27}$	− 0.84	− 0.99	− 1.01	0.86	0.85	$0.384^{+0.511}_{-0.876}$	$0.213^{+0.529}_{-0.760}$	$0.11^{+0.09}_{-0.08}$	$0.09^{+0.06}_{-0.06}$	45.184	45.804
J0143−0056	J014334.89−005635.3	45.534	8.83	$8.65^{+0.27}_{-0.21}$	$8.66^{+0.28}_{-0.23}$	− 0.03	$0.18^{+0.29}_{-0.34}$	$0.16^{+0.31}_{-0.33}$	− 0.95	− 0.88	− 0.85	0.85	0.85	$0.687^{+0.289}_{-1.005}$	$0.768^{+0.223}_{-0.988}$	$0.04^{+0.06}_{-0.04}$	$0.05^{+0.06}_{-0.05}$	45.151	45.817
J0927+0004	J092715.49+000401.1	45.514	9.25	$9.06^{+0.27}_{-0.37}$	$9.06^{+0.26}_{-0.37}$	− 0.36	$-0.15^{+0.37}_{-0.31}$	$-0.15^{+0.36}_{-0.30}$	− 1.38	− 1.28	− 1.27	0.85	0.85	$0.972^{+0.053}_{-0.278}$	$0.976^{+0.050}_{-0.221}$	$0.05^{+0.06}_{-0.05}$	$0.05^{+0.06}_{-0.05}$	45.430	45.730
J0213−0036	J021310.33−003620.5	45.487	8.92	$8.74^{+0.26}_{-0.22}$		− 0.15	$0.19^{+0.30}_{-0.33}$		− 1.09	− 1.06		0.85		$0.468^{+0.454}_{-0.937}$		$0.07^{+0.09}_{-0.07}$		45.322	45.738
J1050+0207	J105057.09+020708.5	45.402	9.01	$8.57^{+0.41}_{-0.32}$		− 0.60	$0.14^{+0.38}_{-0.42}$		− 1.21	− 0.84		0.84		$0.673^{+0.308}_{-0.873}$		$0.06^{+0.07}_{-0.06}$		45.640	45.820
J0948+0137	J094801.42+013716.2	45.317	8.83	$8.69^{+0.24}_{-0.29}$	$8.63^{+0.28}_{-0.31}$	− 0.64	$0.00^{+0.35}_{-0.29}$	$0.06^{+0.36}_{-0.33}$	− 1.15	− 1.12	− 0.96	0.85	0.85	$0.633^{+0.295}_{-0.467}$	$0.704^{+0.261}_{-0.495}$	$0.14^{+0.12}_{-0.11}$	$0.17^{+0.09}_{-0.12}$	45.295	45.398
J0042+0008	J004213.01+000807.3	45.260	8.52	$8.36^{+0.25}_{-0.23}$	$8.48^{+0.16}_{-0.12}$	− 0.14	$0.04^{+0.30}_{-0.33}$	$-0.02^{+0.21}_{-0.25}$	− 0.91	− 0.83	− 1.18	0.85	0.85	$0.451^{+0.481}_{-0.944}$	$-0.090^{+0.702}_{-0.601}$	$0.04^{+0.07}_{-0.05}$	$0.01^{+0.04}_{-0.02}$	45.029	45.429
J1013+0245	J101325.50+024521.5	45.210	9.47	$8.82^{+0.52}_{-0.38}$	$8.81^{+0.49}_{-0.38}$	− 1.10	$-0.29^{+0.42}_{-0.49}$	$-0.30^{+0.45}_{-0.46}$	− 1.89	− 1.38	− 1.40	0.84	0.84	$0.864^{+0.147}_{-1.054}$	$0.845^{+0.165}_{-1.073}$	$0.07^{+0.10}_{-0.07}$	$0.08^{+0.07}_{-0.06}$	45.521	45.300
J1021−0027	J102122.23−002723.6	45.059	9.19	$9.15^{+0.32}_{-0.37}$		− 0.57	$-0.45^{+0.41}_{-0.34}$		− 1.77	− 1.84		0.85		$0.880^{+0.131}_{-0.819}$		$0.39^{+0.09}_{-0.15}$		45.618	45.379
J0038−0019	J003854.41−001926.0	45.021	8.49	$8.51^{+0.19}_{-0.19}$	$8.45^{+0.21}_{-0.17}$	− 0.21	$-0.28^{+0.28}_{-0.27}$	$-0.23^{+0.29}_{-0.29}$	− 1.08	− 1.31	− 1.19	0.86	0.85	$0.433^{+0.488}_{-0.904}$	$0.461^{+0.394}_{-0.873}$	$0.14^{+0.11}_{-0.10}$	$0.15^{+0.08}_{-0.08}$	44.782	45.589
J0912−0040	J091216.68−004046.4	45.011	8.64	$8.47^{+0.26}_{-0.30}$	$8.32^{+0.39}_{-0.31}$	− 0.34	$-0.28^{+0.36}_{-0.33}$	$-0.18^{+0.42}_{-0.44}$	− 1.25	− 1.34	− 1.01	0.85	0.85	$0.249^{+0.634}_{-0.844}$	$0.484^{+0.477}_{-1.000}$	$0.09^{+0.12}_{-0.08}$	$0.15^{+0.11}_{-0.10}$	44.871	44.955
J1048−0019	J104807.57−001943.3	44.947	8.24	$8.21^{+0.19}_{-0.23}$	$8.34^{+0.12}_{-0.12}$	− 0.08	$-0.25^{+0.30}_{-0.27}$	$-0.35^{+0.21}_{-0.20}$	− 0.90	− 1.10	− 1.40	0.86	0.87	$0.102^{+0.708}_{-0.737}$	$-0.234^{+0.643}_{-0.541}$	$0.08^{+0.09}_{-0.07}$	$0.03^{+0.07}_{-0.04}$	44.713	44.967
J1045−0047	J104549.63−004755.3	44.862	8.23	$8.34^{+0.16}_{-0.21}$	$8.40^{+0.13}_{-0.16}$	− 0.29	$-0.29^{+0.31}_{-0.24}$	$-0.33^{+0.29}_{-0.22}$	− 0.95	− 1.31	− 1.43	0.87	0.88	$-0.070^{+0.774}_{-0.641}$	$-0.206^{+0.700}_{-0.571}$	$0.16^{+0.12}_{-0.11}$	$0.15^{+0.13}_{-0.11}$	44.361	44.852
J0042−0011	J004230.44−001102.3	44.806	7.69	$7.91^{+0.15}_{-0.18}$	$7.96^{+0.12}_{-0.14}$	0.37	$-0.07^{+0.30}_{-0.25}$	$-0.08^{+0.29}_{-0.23}$	− 0.43	− 0.66	− 0.76	0.88	0.89	$-0.147^{+0.800}_{-0.613}$	$-0.282^{+0.694}_{-0.533}$	$0.22^{+0.09}_{-0.09}$	$0.23^{+0.10}_{-0.10}$	44.785	45.114
J1046+0025	J104629.66+002538.9	44.757	8.17	$8.17^{+0.18}_{-0.23}$	$8.16^{+0.18}_{-0.22}$	− 0.16	$-0.40^{+0.31}_{-0.26}$	$-0.39^{+0.31}_{-0.26}$	− 0.95	− 1.22	− 1.20	0.86	0.86	$0.008^{+0.764}_{-0.675}$	$0.023^{+0.747}_{-0.681}$	$0.09^{+0.10}_{-0.08}$	$0.09^{+0.10}_{-0.08}$	44.310	44.848
J0930−0018	J093046.79−001825.8	44.701	8.55	$8.47^{+0.23}_{-0.28}$		− 0.49	$-0.56^{+0.34}_{-0.30}$		− 1.36	− 1.63		0.85		$0.228^{+0.624}_{-0.818}$		$0.14^{+0.15}_{-0.11}$		44.416	44.704
J1108+0141	J115841.37−032239.9	46.337	9.37			0.74			− 0.59									44.625	
J1005+0245	J100513.75+024510.3	46.062	9.45			0.52			− 1.07									44.570	

Note. [a]Based on the best-fitting model to the X-shooter spectrum.

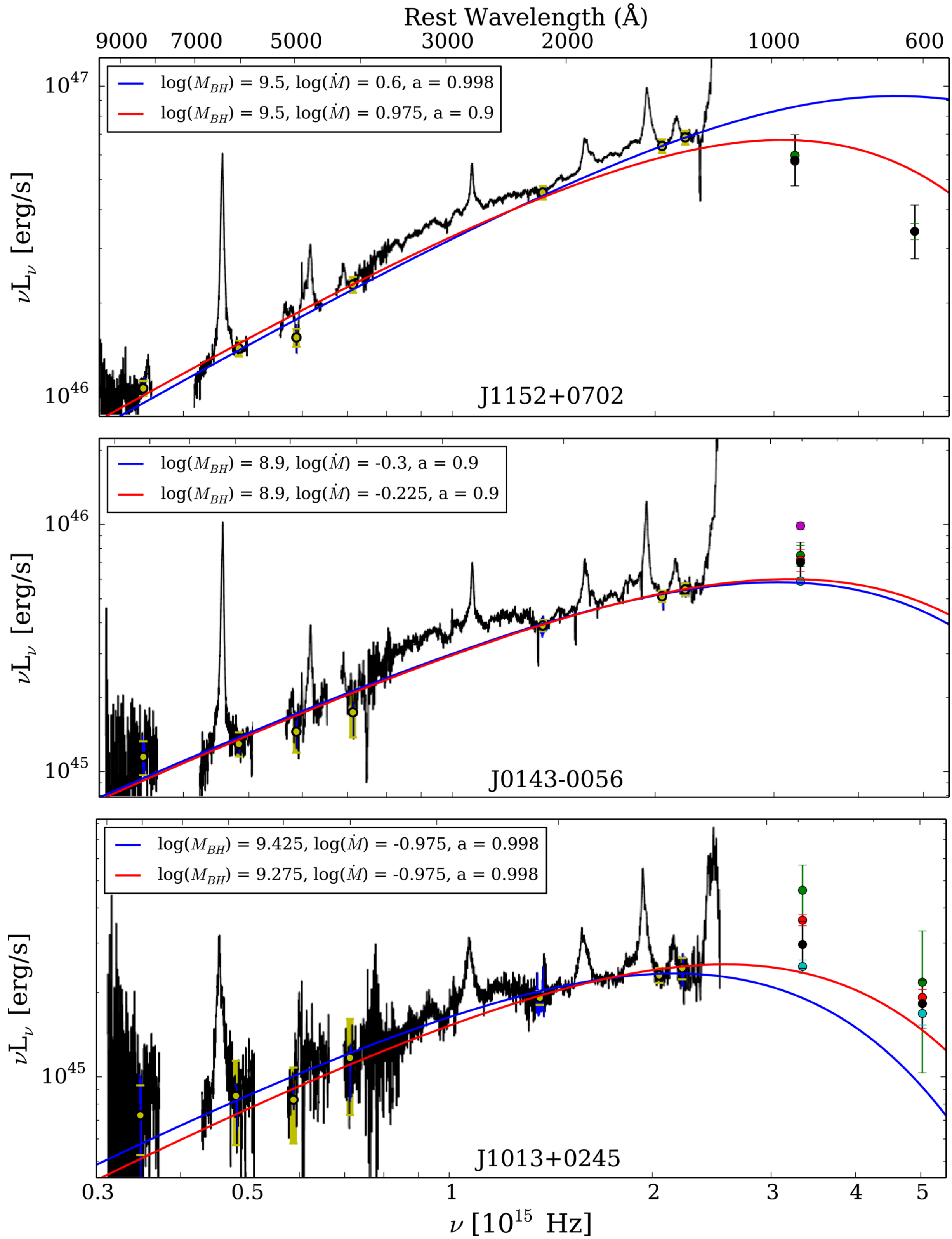

Figure 4. Examples of satisfactory fits to the combined X-shooter+*GALEX* SED. The blue curve is the best fit to just the X-shooter spectrum, and the red curve is the best fit to X-shooter+*GALEX*. The coloured points are the individual *GALEX* epochs, and the black points are the weighted average of the different epochs.

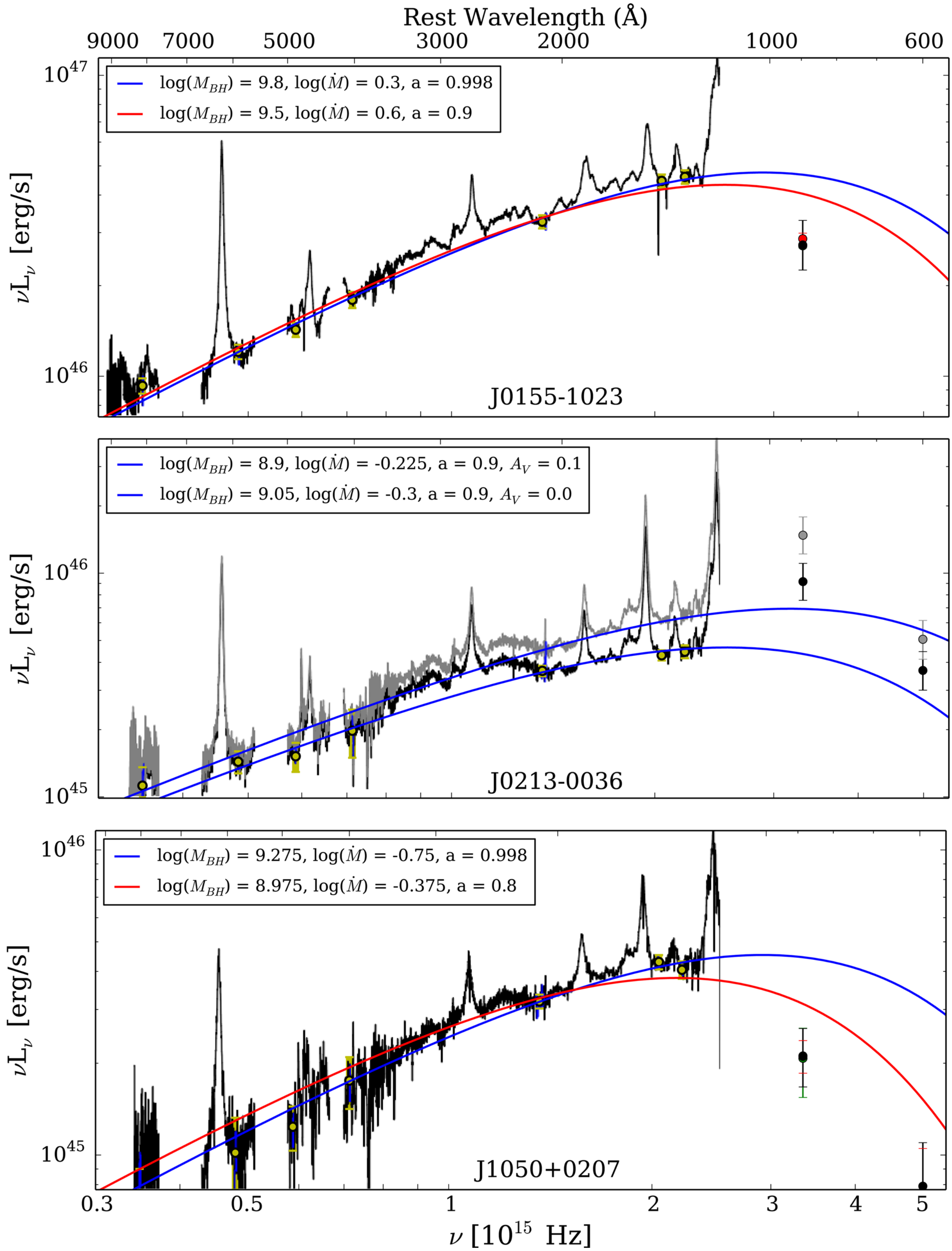

Figure 5. Same as Fig. 4, but for cases where no satisfactory fit was found to the X-shooter+*GALEX* SED. For J0213−0036, we show just the fits to the X-shooter+*GALEX* SED, for before and after applying an intrinsic reddening correction. The grey curve and points are the dereddened SED.

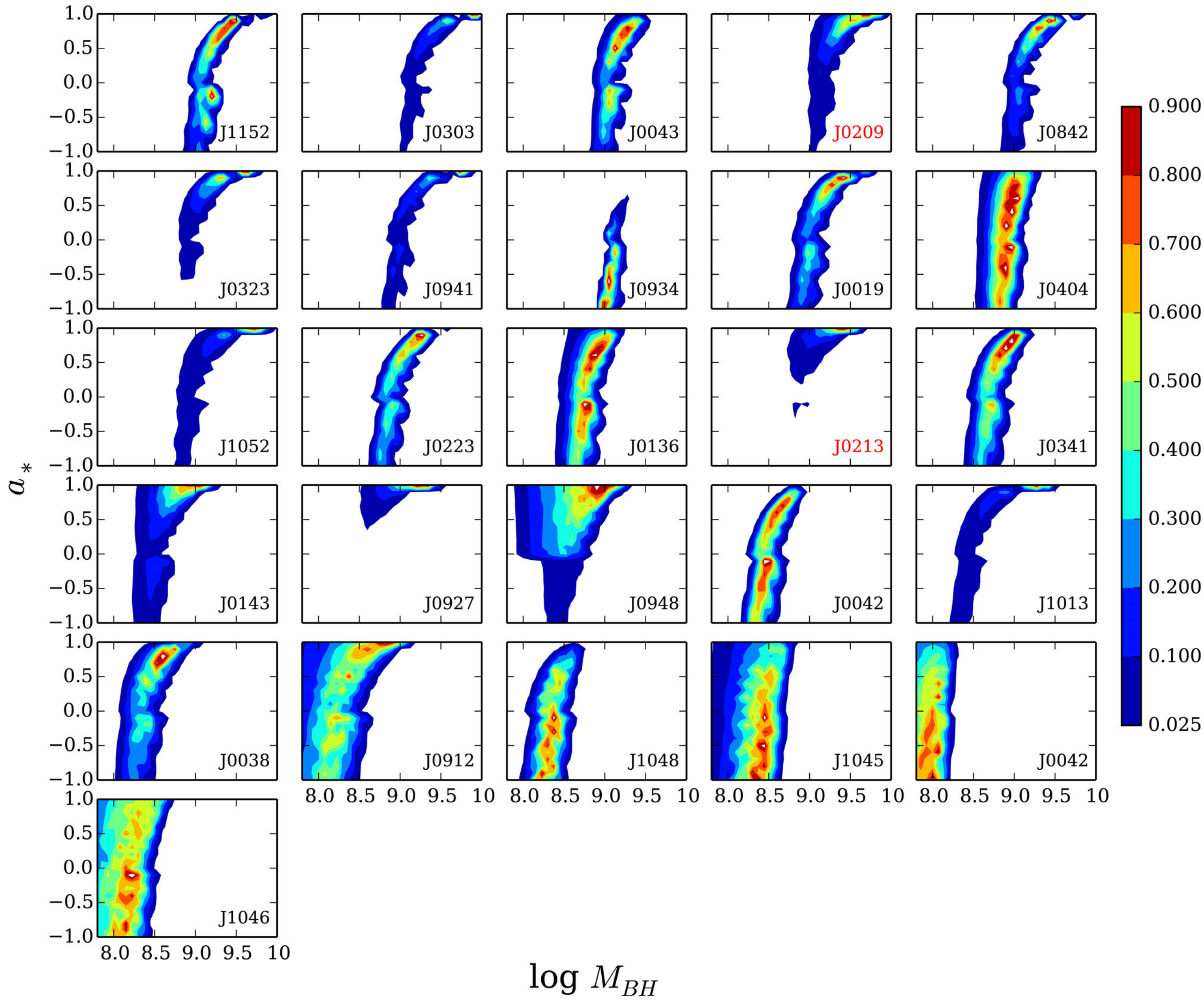

Figure 6. Same as Fig. 3, but for fits to the combined X-shooter+*GALEX* SEDs.

black points are the weighted average of all the epochs. Fig. 4 shows three examples of satisfactory fits, and Fig. 5 shows three examples of cases with a marginal fit or with clearly no fit at all. We are able to find satisfactory fits to 26/38 of the combined X-shooter+*GALEX* SEDs.

Just as in Section 3.3, we consider intrinsic reddening when fitting the X-shooter+*GALEX* SEDs. However, we find that correcting for intrinsic reddening does not solve the discrepancy we find between the models and the *GALEX* photometry for the objects that have satisfactory fits to X-shooter alone. There are just two sources whose X-shooter+*GALEX* SEDs are fit only with $A_V > 0$, but these are two of the sources that already required dereddening for a satisfactory fit to the X-shooter spectrum alone.

The examples in Fig. 4, in particular J0143−0056 and J1013+0245, show how variability between the X-shooter and *GALEX* epochs can cause the difference between a good and a bad fit. For example, the magenta *GALEX* point for J0143−0056 and the green points for J1013+0245 would not be fit with the thin AD model. If we only had those epochs available, then these two objects would not be considered to have satisfactory fits. If we had contemporaneous UV data for J1050+0207 (Fig. 5), for example, it is possible that we would find a satisfactory fit to the entire SED. Therefore, we can see from many of the objects with multi-epoch *GALEX* data that the unknown variability between the X-shooter and *GALEX* epochs is a real uncertainty, and the fraction with satisfactory fits (26/38) is likely a lower limit.

It is also instructive to examine in how many cases our 'best-fitting' models overestimate and underestimate the *GALEX* luminosities. If the discrepancies between the model and the *GALEX* measurements are due primarily to variability, then one would expect to find roughly the same number of cases where the model overestimates these measurements versus the number where the model underestimates these measurements. Considering the best-fitting model to just the X-shooter spectrum, roughly the same number overestimate the *GALEX* photometry versus underestimate (11 versus 9 sources). Similarly, when fitting the X-shooter+*GALEX* SED, half of the best-fitting models overestimate the *GALEX* luminosities and half underestimate. For this comparison, we are considering just the weighted average of the *GALEX* measurements. These results show that the thin AD model does not systematically overestimate or underestimate the *GALEX* data.

As in Section 3.3, we plot the a_* versus $M_{\rm BH}$ probability contours for fitting the thin AD models now to the X-shooter+*GALEX* SED in Fig. 6. The constraints on the spin are less confined for many sources when including the *GALEX* photometry in the fitting, especially for the AGN with higher $M_{\rm BH}$, e.g. J1152+0702. For some of these high mass cases, the contours are shifted to lower spin parameters than when fitting the X-shooter spectrum alone.

4 DISCUSSION

4.1 AGN accretion discs

In this work, we fit standard thin AD models (Section 3.1) to X-shooter spectra of 39 AGN at $z \sim 1.5$ and also to the combined X-shooter+*GALEX* SED of 38 of these sources. When considering just the X-shooter spectrum, we can fit 37 out of 39 AGN spectra in our sample when allowing for a small intrinsic reddening correction. Collinson et al. (2015) also find agreement between the thin AD model and the optical/IR spectra for many of their 11 sources.

When including *GALEX* photometry in our fitting procedure, the number of AGN that we can fit satisfactorily is reduced to 26 out of 38 AGN. Accurately fitting SEDs to X-shooter and *GALEX* data is hampered by potential variability between the X-shooter and *GALEX* epochs. For the sample overall, in roughly half the cases where we do not find a model fit that is consistent with both the X-shooter spectrum and the *GALEX* photometry, the model fit overestimates the *GALEX* measurements (see Section 3.4). Therefore, there is an even split between overestimating and underestimating the *GALEX* measurements, indicating that variability is a likely cause for the discrepancy between model and observations for the 11 sources that no longer have a satisfactory thin AD model fit.

However, if we consider just the AGN with $M_{\rm BH} > 10^9$ M$_\odot$, and ignore the two AGN with broad absorption, the tendency is for the model to overestimate the *GALEX* photometry for those cases with no satisfactory fit. This at least suggests that the discrepancy between the thin AD model and the *GALEX* photometry might not be due solely to variability between the *GALEX* and X-shooter epochs, at least for the brighter half of the sample, but rather that there is some physical explanation for the discrepancy.

While we found both in Paper I and in the current work that an intrinsic reddening correction can cure discrepancies between the model and the X-shooter spectrum in the bluer part of the X-shooter spectrum, we do not find that intrinsic reddening helps to cure the discrepancies between the model and the *GALEX* photometry mentioned above when our models overestimate the *GALEX* luminosities.

One possibility for the discrepancy at short wavelengths is outflowing gas from the accretion disc. Both Slone & Netzer (2012) and Laor & Davis (2014) show how including a mass outflow from a thin AD reduces the radiation at shorter wavelengths, and this could explain the discrepancy between the data and the model for those cases where the model overestimates the *GALEX* photometry.

Another further possibility is that some of these systems do not harbour a thin AD, but rather a 'slim' accretion disc. Such discs are expected at larger $L/L_{\rm Edd}$ ($L/L_{\rm Edd} > \sim 0.2$; Abramowicz et al. 1988; Ohsuga & Mineshige 2011; Netzer 2013; Wang et al. 2014). However, current models of 'slim' discs are not yet able to produce predicted SEDs that are accurate enough for a comparison to observed SEDs as we perform in this work (see e.g. Sadowski & Narayan 2016). It will be informative to compare such model SEDs, when they are available, to data sets like the one presented here to test what fraction of AGN are consistent with having a 'slim' AD.

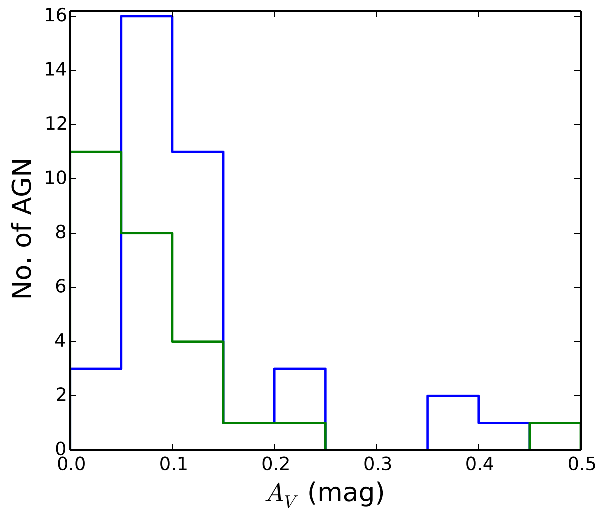

Figure 7. The distribution in the median A_V values from the Bayesian fitting procedure. The blue curve is based on fits to the X-shooter spectra alone, and the green curve is based on fits to the combined X-shooter+*GALEX* SED.

4.2 Reddening in AGN host galaxies

In Paper I, we compared three different extinction curves – simple power-law, Galactic, and SMC – and found that the simple power-law and Galactic curves gave the best fits to the observed SEDs. In this paper, to reduce the number of free parameters in our Bayesian fitting procedure, we only consider the simple power-law model, but we can compare our results to the typical amount of reddening found in AGN in other work.

In Fig. 7, we plot the distribution in A_V values from our Bayesian fitting routine for all the AGN with satisfactory thin AD fits. Most of the AGN have A_V values $\leq$0.15 mag. For comparison, Krawczyk et al. (2015) find that just 2.5 per cent of non-BAL quasars, out of a large sample of SDSS quasars, have $A_V > 0.3$ mag. In our smaller sample, the results of our Bayesian fitting routine gives 2 out of 37 non-BAL AGN (5 per cent) with $A_V > 0.3$ mag. This is generally consistent with the results of Krawczyk et al. (2015) and indicates that, in general, we are not overcorrecting the spectra when including intrinsic reddening as a parameter in the fitting routine.

While our sample was selected to avoid AGN with significant absorption, there are two sources in the sample with BAL absorption (J1005+0245 and J1021−0027). We could not find satisfactory fits for either of these two sources before intrinsic reddening correction, even when fitting the X-shooter spectrum alone. After correcting for intrinsic reddening, we find a satisfactory fit for one and a marginal fit for the other. This is consistent with previous work that has shown that BAL quasars tend to have redder spectra than non-BAL quasars. For example, Krawczyk et al. (2015) find that 13 per cent of BAL quasars have $A_V > 0.3$ mag, compared to just 2.5 per cent of non-BAL quasars, as mentioned above. One of the BAL AGN in our sample, J1021−0027, has $A_V = 0.39^{+0.09}_{-0.15}$ mag. The other, J1005+0245, does not have a satisfactory thin AD fit, but the closest fit we find is with an $A_V = 0.50$ mag.

4.3 Disc-derived $M_{\rm BH}$ and $L/L_{\rm Edd}$ and bolometric correction factors

Given the fitted thin AD SEDs, we can now compare the values of $M_{\rm BH}$ and $L/L_{\rm Edd}$ derived from the thin AD fits to our best estimates

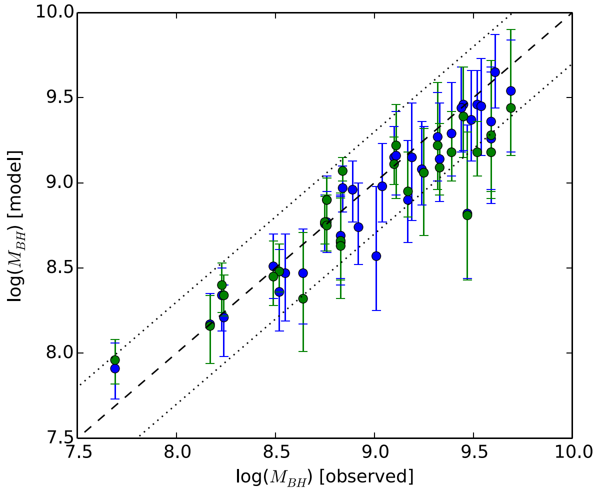

Figure 8. A comparison between the observed $M_{\rm BH}$, measured in Paper II directly from the spectra, and the median value of $M_{\rm BH}$ from the Bayesian fitting procedure for just the X-shooter spectra (blue points) and for the combined X-shooter+*GALEX* SED (green points). For reference, the dashed line is the one-to-one line, and the dotted lines are ±0.3 dex. The typical error on $\log(M_{\rm BH}^{\rm obs})$ is 0.3 dex.

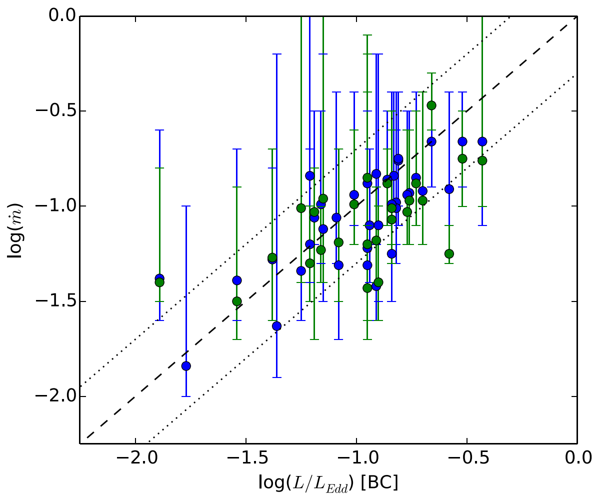

Figure 9. Same as Fig. 8, but instead showing a comparison between $L/L_{\rm Edd}$[BC], calculated directly from the observed spectra using a bolometric correction (BC) factor (Paper II), and the median $\dot{m}$ value from the Bayesian fitting routine. The typical errors on $L/L_{\rm Edd}$ are at least as high as those on $M_{\rm BH}^{\rm obs}$.

of $M_{\rm BH}$ and $L/L_{\rm Edd}$ derived directly from the observed spectrum (Paper II). In particular, Fig. 8 shows that we are able to find satisfactory fits for most of the AGN in our sample with thin AD models that have BH masses within $\sim 1\sigma$ of the observed values of $M_{\rm BH}$. Interestingly, we also find good agreement between $L/L_{\rm Edd}$[BC], which is measured directly from the observed spectrum using a bolometric correction (BC) factor, and the median value of $L/L_{\rm Edd}$ ($\dot{m}$) from our thin AD fitting procedure, as shown in Fig. 9. Comparing Figs 8 and 9 to the corresponding figures in Paper I, it is clear that we find better agreement here between the results of the Bayesian analysis and the observationally derived quantities, especially between $\dot{m}$ and $L/L_{\rm Edd}$[BC]. This is largely due to the improvements in the measurements of $M_{\rm BH}$, as described in Paper II. In Paper I, we see a systematic offset between $\dot{m}$ and $L/L_{\rm Edd}$. The $M_{\rm BH}$ estimates used here are systematically larger than in Paper I, thus reducing the values of $L/L_{\rm Edd}$[BC] and bringing them more in line with our estimates of $\dot{m}$ from the thin AD fitting.

The inputs to the Bayesian fitting procedure are $M_{\rm BH}$ and $\dot{M}$, as measured from the spectra, neither of which require a bolometric correction to calculate. On the other hand, calculating $L/L_{\rm Edd}$ directly from the spectra requires a bolometric correction, and the good agreement between $\dot{m}$ and $L/L_{\rm Edd}$ found here in Fig. 9 indicates that the bolometric correction factors used in Paper II to calculate $L/L_{\rm Edd}$ give reasonable results.

4.4 Black hole spin

The goal of the spectral fitting is not just to test the thin AD theory, but in cases where the observed data is consistent with the theory, to attempt to constrain a_*, as demonstrated already in Paper I. With our results, we see that we can obtain much tighter constraints for active BHs above $M_{\rm BH} \sim 10^9$ M$_\odot$, as compared to those below this mass. This tendency is expected since precise determination of the spin parameter depends, crucially, on the wavelength range exhibiting the largest SED curvature. This range is at longer wavelengths for more massive BHs and BHs with lower $L/L_{\rm Edd}$. For the most massive objects in our sample, this range is well inside the X-shooter wavelength coverage, and hence we can better constrain a_*. For lower mass, higher accretion rate BHs, much of the curvature is at far-UV wavelengths, and the X-shooter range can thus be fitted by a range of models with a wide range in a_*. Fig. 10 combines the results presented in Figs 3 and 6 and Table 3, and it is clear that the most massive BHs have both the highest spin parameters and the tightest constraints on the spin parameter.

If we focus on the 17 sources with $M_{\rm BH} > 10^9$ M$_\odot$ and $a_* > 0.7$ (efficiency ~ 0.1), when fitting just the X-shooter spectrum, 10 of those have a satisfactory fit with *GALEX*. Of these 10, the estimate of a_* decreases to below 0.7 for 5 of them after fitting the X-shooter+*GALEX* SED, and the errors on a_* are larger. This reduction in spin parameter is due to the *GALEX* photometry forcing the fits to lower luminosities at far-UV wavelengths.

We also see that while *GALEX* provides some crucial information on the SED shape bluewards of ∼1200 Å for our sample, it does not, in general, reduce the uncertainties on the parameters involved in fitting the thin AD model. As mentioned already, our spin parameter estimates for the highest mass BHs are now more uncertain, and the uncertainty on the spin for the BHs with $M_{\rm BH} < 10^9$ M$_\odot$ is similar after including *GALEX*. This is likely due mostly to the large uncertainties on the *GALEX* points. If the ‘turnover’ in the thin AD spectrum occurs shortwards of 1200 Å, then spectra are needed in this wavelength regime to properly trace the SED and fit the thin AD models. Follow-up spectroscopy with *HST* is thus necessary to confidently test the thin AD model and obtain more precise constraints on the BH spin.

Despite the uncertainties mentioned above, the results still give some insight into the evolution of SMBH spin in AGN. The two commonly discussed scenarios in the literature to characterize this evolution are referred to as ‘spin-up’ and ‘spin-down’. The difference between these two scenarios is primarily in the nature of the accretion episodes that fuel the BH. On the one hand, a series of accretion episodes with random and isotropic orientations will cause the SMBH to ‘spin-down’ to moderate spins near $a_* \sim 0$, regardless of the final mass of the SMBH (King, Pringle & Hofmann 2008; Wang et al. 2009; Li, Wang & Ho 2012; Dotti et al. 2013). On the other hand, growing a SMBH via a single prolonged accretion

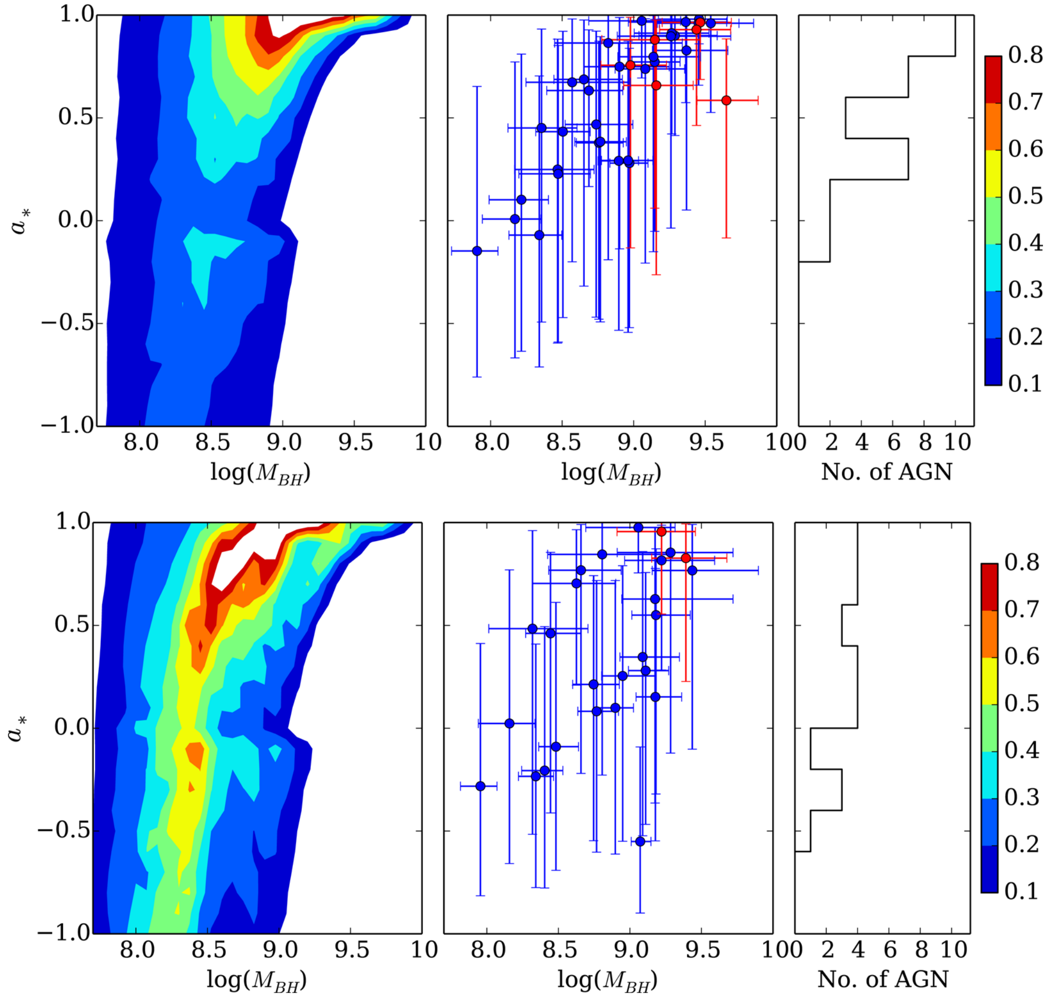

Figure 10. The spin parameter, a_*, as a function of $M_{\rm BH}$. Top panel is based on fits to X-shooter only (37 sources), and the bottom panel is based on fits to X-shooter+*GALEX* (26 sources). The left-hand panel is a contour plot of the combined probability distributions in a_* and $M_{\rm BH}$ for the sources with satisfactory fits. The middle panel shows the median a_* and $M_{\rm BH}$ values, with the red points identifying those sources for which dereddening was required for a satisfactory thin AD fit. The right-hand panel shows the distribution in the best-fitting spin parameters.

episode, or for the most massive BHs, when the orientations of the accretion episodes have even a small amount of anisotropy, the SMBH will 'spin-up' to a high spin parameter (Dotti et al. 2013; Volonteri et al. 2013).

In Paper I, we found that our results favour the 'spin-up' scenario, and our current results favour this scenario for similar reasons. We again find a wide range in spin parameters for the sample, as shown in the rightmost panels of Fig. 10, with the exception that there are almost no sources with $a_* < -0.5$. Furthermore, even with the *GALEX* points included in the analysis, there are many sources with high spin ($a_* > \sim 0.5$). If the 'spin-down' scenario were dominating, i.e. if there were multiple, randomly-oriented accretion events throughout the lifetime of these SMBHs, we would expect a concentration of values around $a_* \sim 0$. Instead, our results favour scenarios where there is just one long accretion episode or multiple events with some preferred orientation.

In fact, compared to Paper I, we see a clear shift in the distribution of a_* towards higher spin. This is due both to the higher black hole mass estimates (see Section 3.1 and Paper II) and to the inclusion of an intrinsic reddening correction in the Bayesian fitting procedure. While for most objects the typical amount of intrinsic reddening is small ($A_V < 0.15$ mag), any correction of the spectrum for reddening will increase the luminosity at shorter wavelengths much more than at the longest wavelengths in the SED. This will favour higher spin parameters, if all other parameters remain roughly the same. Previous efforts to constrain BH spin have also generally concluded that many BHs have high spin, especially the most massive ($M_{\rm BH} > 10^9$ M$_\odot$) BHs (Davis & Laor 2011; Reis et al. 2014; Reynolds 2014; Reynolds et al. 2014; Trakhtenbrot 2014; Wang et al. 2014). All of this supports the 'spin-up' scenario of BH spin evolution.

5 CONCLUSIONS

This work is the third in a series of papers describing the spectroscopic properties of a sample of AGN at $z \sim 1.5$, selected to cover a wide range in both $M_{\rm BH}$ ($\sim 10^8$ to 10^{10} M$_\odot$) and $L/L_{\rm Edd}$[BC] ($\sim$0.01 to 0.4) and observed with the X-shooter instrument, which provides very wide, single-epoch coverage. We apply a similar, but improved, Bayesian procedure as in Paper I to fit thin AD models to observed AGN SEDs, this time with a larger sample (39 AGN), improved $M_{\rm BH}$ estimates from Paper II, and the inclusion of intrinsic reddening as a parameter in our Bayesian SED fitting procedure.

When fitting the thin AD model to the X-shooter spectra alone, we find that we are able to fit more of the AGN in our sample than in Paper I, with 37 out of 39 AGN (95 per cent) having a satisfactory fit (Section 3.3). For those AGN with satisfactory fits, we constrain the spin parameter, a_*, with the constraints becoming less well-defined with decreasing $M_{\rm BH}$. The distribution in a_* for these sources ranges from negative spin to nearly maximum spin. This distribution tends to favour the 'spin-up' scenario of BH spin evolution, suggesting that these AGN are generally fueled by relatively long episodes of coherent accretion with some preferred orientation (Section 4.4).

We also investigate the inclusion of non-simultaneous *GALEX* photometry in our analysis. This decreases the number with satisfactory fits to 26 out of 38 (68 per cent) sources (Section 3.4); however, given the large variability that can occur for AGN at these UV wavelengths, it is unclear how much variability is affecting our fitting results for these combined X-shooter+*GALEX* SEDs. The inclusion of *GALEX* photometry also tends to decrease the estimates of a_*, especially for the AGN with larger $M_{\rm BH}$, but taken at face value, these estimates of a_* still support the 'spin-up' scenario of BH spin evolution.

While our results support the thin AD theory for a majority of the AGN in our sample, simultaneous UV and optical spectra are required to properly test the thin AD theory in the far-UV, where, for many sources, the peak of the thin AD spectrum occurs. Such simultaneous spectra will also provide the best constraints on a_*, particularly for the lower $M_{\rm BH}$ sources.

ACKNOWLEDGEMENTS

We thank the anonymous referee for helpful comments on the manuscript. We thank the DFG for support via German Israeli Cooperation grant STE1869/1-1.GE625/15-1. Funding for this work has also been provided by the Israel Science Foundation grant number 284/13. HN acknowledges useful discussions and local support from the International Space Science Institute (ISSI), in Bern, during a work-group meeting in 2015.

REFERENCES

Abazajian K. N. et al., 2009, ApJS, 182, 543
Abramowicz M. A., Czerny B., Lasota J. P., Szuszkiewicz E., 1988, ApJ, 332, 646
Banerji M. et al., 2015, MNRAS, 454, 419
Bongiorno A. et al., 2014, MNRAS, 443, 2077
Brenneman L., 2013, Measuring the Angular Momentum of Supermassive Black Holes. Springer, Berlin
Bruzual G., Charlot S., 2003, MNRAS, 344, 1000
Capellupo D. M., Netzer H., Lira P., Trakhtenbrot B., Mejía-Restrepo J., 2015, MNRAS, 446, 3427 (Paper I)
Cardelli J. A., Clayton G. C., Mathis J. S., 1989, ApJ, 345, 245
Collin S., Boisson C., Mouchet M., Dumont A.-M., Coupé S., Porquet D., Rokaki E., 2002, A&A, 388, 771
Collinson J. S., Ward M. J., Done C., Landt H., Elvis M., McDowell J. C., 2015, MNRAS, 449, 2174
Croom S. M. et al., 2009, MNRAS, 392, 19
Davis S. W., Laor A., 2011, ApJ, 728, 98
Done C., Davis S. W., Jin C., Blaes O., Ward M., 2012, MNRAS, 420, 1848
Dotti M., Colpi M., Pallini S., Perego A., Volonteri M., 2013, ApJ, 762, 68
Fabian A. C., Iwasawa K., Reynolds C. S., Young A. J., 2000, PASP, 112, 1145
Freudling W., Romaniello M., Bramich D. M., Ballester P., Forchi V., García-Dabló C. E., Moehler S., Neeser M. J., 2013, A&A, 559, A96
Hubeny I., Blaes O., Krolik J. H., Agol E., 2001, ApJ, 559, 680
King A. R., Pringle J. E., Hofmann J. A., 2008, MNRAS, 385, 1621
Koratkar A., Blaes O., 1999, PASP, 111, 1
Krawczyk C. M., Richards G. T., Gallagher S. C., Leighly K. M., Hewett P. C., Ross N. P., Hall P. B., 2015, AJ, 149, 203
Laor A., Davis S. W., 2014, MNRAS, 438, 3024
Li Y.-R., Wang J.-M., Ho L. C., 2012, ApJ, 749, 187
MacLeod C. L. et al., 2012, ApJ, 753, 106
McLure R. J., Dunlop J. S., 2004, MNRAS, 352, 1390
Mathis J. S., Rumpl W., Nordsieck K. H., 1977, ApJ, 217, 425
Mejía-Restrepo J. E., Trakhtenbrot B., Lira P., Netzer H., Capellupo D. M., 2016, MNRAS, 460, 187 (Paper II)
Modigliani A. et al., 2010, in Silva D. R., Peck A. B., Soifer B. T., eds, Proc. SPIE Conf. Ser. Vol. 7737, Observatory Operations: Strategies, Processes, and Systems III. SPIE, Bellingham, p. 773728
Morrissey P. et al., 2007, ApJS, 173, 682
Netzer H., 2013, The Physics and Evolution of Active Galactic Nuclei.
Ohsuga K., Mineshige S., 2011, ApJ, 736, 2
Reis R. C., Reynolds M. T., Miller J. M., Walton D. J., 2014, Nature, 507, 207
Reynolds C. S., 2014, Space Sci. Rev., 183, 277
Reynolds C. S., Lohfink A. M., Babul A., Fabian A. C., Hlavacek-Larrondo J., Russell H. R., Walker S. A., 2014, ApJ, 792, L41
Risaliti G. et al., 2013, Nature, 494, 449
Sadowski A., Narayan R., 2016, MNRAS, 456, 3929
Schlegel D. J., Finkbeiner D. P., Davis M., 1998, ApJ, 500, 525
Shakura N. I., Sunyaev R. A., 1973, A&A, 24, 337
Shen Y. et al., 2011, ApJS, 194, 45
Slone O., Netzer H., 2012, MNRAS, 426, 656
Stern J., Laor A., 2012, MNRAS, 423, 600
Trakhtenbrot B., 2014, ApJ, 789, L9
Trakhtenbrot B., Netzer H., 2012, MNRAS, 427, 3081
Vernet J. et al., 2011, A&A, 536, A105
Volonteri M., Sikora M., Lasota J.-P., Merloni A., 2013, ApJ, 775, 94
Wang J.-M. et al., 2009, ApJ, 697, L141
Wang J.-M. et al., 2014, ApJ, 793, 108
Zuo W., Wu X.-B., Liu Y.-Q., Jiao C.-L., 2012, ApJ, 758, 104

This paper has been typeset from a TEX/LATEX file prepared by the author.